ANNUAL REVIEWS

Annual Review of Control, Robotics, and Autonomous Systems

Stochastic Dynamical Modeling of Turbulent Flows

A. Zare,[1] T.T. Georgiou,[2] and M.R. Jovanović[3]

[1]Department of Mechanical Engineering, University of Texas at Dallas, Richardson, Texas 75080, USA

[2]Department of Mechanical and Aerospace Engineering, University of California, Irvine, California 92697, USA

[3]Ming Hsieh Department of Electrical and Computer Engineering, University of Southern California, Los Angeles, California 90089, USA; email: mihailo@usc.edu

ANNUAL REVIEWS CONNECT

www.annualreviews.org

- Download figures
- Navigate cited references
- Keyword search
- Explore related articles
- Share via email or social media

Abstract

Advanced measurement techniques and high-performance computing have made large data sets available for a range of turbulent flows in engineering applications. Drawing on this abundance of data, dynamical models that reproduce structural and statistical features of turbulent flows enable effective model-based flow control strategies. This review describes a framework for completing second-order statistics of turbulent flows using models based on the Navier–Stokes equations linearized around the turbulent mean velocity. Dynamical couplings between states of the linearized model dictate structural constraints on the statistics of flow fluctuations. Colored-in-time stochastic forcing that drives the linearized model is then sought to account for and reconcile dynamics with available data (that is, partially known statistics). The number of dynamical degrees of freedom that are directly affected by stochastic excitation is minimized as a measure of model parsimony. The spectral content of the resulting colored-in-time stochastic contribution can alternatively arise from a low-rank structural perturbation of the linearized dynamical generator, pointing to suitable dynamical corrections that may account for the absence of the nonlinear interactions in the linearized model.

1. INTRODUCTION

Turbulent flows are at the center of many key processes in nature and in engineering applications. Energy dissipation caused by turbulent fluctuations around airplanes, ships, and submarines increases resistance to motion (i.e., skin-friction drag) and fuel consumption and compromises the performance of vehicles. This motivates the design of flow control strategies for the improved performance of air and water vehicles and other systems that involve turbulent flows (1, 2).

Models that are based on the Navier–Stokes (NS) equations capture the dynamics and statistical features of fluid flows. However, these models are given by 3-D nonlinear partial differential equations and involve a number of degrees of freedom that is prohibitively large for analysis and control synthesis (3, 4). Moreover, to this day, a detailed understanding of the mechanisms responsible for the dissipation of energy in turbulent flows is missing. As a result, traditional flow control techniques are largely empirical, and they rely on physical intuition, numerical simulations, and experiments. Even though these techniques provide invaluable insights, they are costly, time-consuming, and not suitable for model-based controller design.

Direct numerical simulation (DNS) offers a computational approach to finding a solution to the NS equations. At moderate Reynolds numbers, DNS provides important insight into structural and statistical features of turbulent flows, but the computational complexity increases roughly as the cube of the Reynolds number, and DNS becomes prohibitively expensive in most flow regimes that are encountered in engineering practice (3). An alternative to DNS has been to either fully resolve large-scale 3-D turbulent flow structures and model the impact of smaller scales or focus on statistical signatures of turbulent flows, i.e., the mean flow components and their higher-order moments. The former approach gives rise to large-eddy simulation, which relies on modeling the impact of small unresolved physical scales (5), and the latter forms the basis for the statistical theory of turbulence (6). While large-eddy simulation accurately captures the large-scale unsteady motions that dominate flows around air and water vehicles, its computational cost is still too high for it to be incorporated into aerodynamic design (4). Since an exact set of dynamical equations that govern the evolution of statistics of turbulent flows does not exist, the statistical theory of turbulence aims to develop approximate mathematical models for turbulent flows (7). Indeed, recent research suggests that conventional techniques can be significantly enhanced using low-complexity models that are convenient for real-time control design and optimization (8).

In general, modeling can be seen as an inverse problem where a search in parameter space aims to identify a parsimonious representation of data. For turbulent flows, the advent of advanced measurement techniques and high-performance parallel computing has resulted in large data sets for a wide range of flow configurations and speeds. Drawing on this abundance of data, one can construct dynamical models to reproduce structural and statistical features of turbulent flows.

The prevalence of coherent structures in turbulent wall-bounded shear flows (9–12) has inspired the development of data-driven techniques for reduced-order modeling of turbulent flows (13–18). However, unreliable measurements and data anomalies challenge a sole reliance on data because such models are agnostic to the underlying physics. Furthermore, control actuation and sensing may significantly alter the identified modes in unpredictable ways. This compromises the performance of data-driven models in regimes that were not accounted for in the training process and introduces nontrivial challenges for model-based control design (19, 20). A promising alternative is to leverage the underlying physics in the form of a prior model that arises from first principles, e.g., linearization of the NS equations around stable flow states. This review highlights recent developments in combining data-driven techniques with systems theory and optimization to enhance the predictive capabilities of physics-based dynamical models.

Over the last three decades, important dynamical aspects of transitional and turbulent flows have been captured by the analysis of the linearized NS equations. Specifically, the nonnormality of the linearized dynamical generator introduces interactions among exponentially decaying normal modes (21, 22). This property has been used to explain high flow sensitivity in the early stages of transition and to identify key mechanisms for subcritical transition to turbulence; even in the absence of modal instability, bypass routes to transition can be triggered by large transient growth (23–27) or large amplification of deterministic and stochastic disturbances (21, 28–32). Similar amplification mechanisms have been observed for the linearized NS equations around the turbulent mean velocity (30, 33–36). Additional insights into the geometric scaling of dominant modes over various flow conditions have been provided by low-order representations resulting from singular value decomposition of the associated frequency response operator (36–38).

The nonlinear terms in the NS equations play an important role in the growth of flow fluctuations, transition to turbulence, and sustaining turbulent flow. Since these terms are conservative, they do not contribute to the transfer of energy between the mean flow and velocity fluctuations, but they do transfer energy between different spatiotemporal Fourier modes (7, 39). This feature has inspired modeling of the effect of nonlinearity using additive forcing to the linearized equations that govern the dynamics of fluctuations. Early efforts in this direction focused on modeling homogeneous isotropic turbulence (40–43). Stochastically forced linearized NS equations were later used to model heat and momentum fluxes as well as spatiotemporal spectra in quasi-geostrophic turbulence (44–46), while structural features of wall-bounded turbulent flows were captured using the spatiotemporal frequency responses of the linearized NS equations (28–31, 36, 47–49). These studies used forcing to model exogenous excitation sources and uncertain initial conditions, as well as to replicate the effects of the nonlinear terms in the full NS equations.

This review explains how stochastic dynamical models can enhance the linearized NS equations to accurately replicate observed statistical features of turbulent flows. This is accomplished by bringing together tools from systems theory and convex optimization in order to suitably shape the power spectrum of additive stochastic forcing into the dynamical equations. We focus on replicating second-order statistics and cast the corresponding model identification as a convex optimization problem. The resulting stochastic component can be linked to a structural (low-rank) perturbation of the dynamical generator, suggesting suitable correction to account for the absence of the nonlinear interactions.

The review is organized as follows. In Section 2, we provide the background on the NS equations and turbulence modeling. In Section 3, we introduce the stochastically forced linearized NS equations and describe structural constraints on admissible state covariances and input power spectra. In Section 4, we demonstrate the necessity for colored-in-time stochastic forcing and formulate a convex optimization problem aimed at matching available and completing unavailable second-order statistics of turbulent flows via low-complexity stochastic dynamical models. In Section 5, we apply the stochastic modeling approach of Section 4 to a turbulent channel flow, verify its utility in linear stochastic simulations, and examine the resulting spatiotemporal spectrum. Finally, we provide concluding remarks in Section 6, which is followed by a summary of key points and outstanding research issues.

2. THE NAVIER–STOKES EQUATIONS

Flows of incompressible Newtonian fluids are governed by the NS and continuity equations

$$
\begin{aligned}
\partial_t \mathbf{u} + (\mathbf{u} \cdot \nabla)\, \mathbf{u} &= -\nabla P + \frac{1}{Re}\, \Delta \mathbf{u}, \\
0 &= \nabla \cdot \mathbf{u},
\end{aligned}
\qquad 1.
$$

where **u** is the velocity vector that satisfies the no-slip and no-penetration boundary conditions at a stationary solid surface; P is the pressure; ∇ and $\Delta = \nabla \cdot \nabla$ are the gradient and Laplacian operators, respectively; and ∂_t is the partial derivative with respect to time. The NS equations are nonlinear partial differential equations in spatial coordinates **x** and time t, and the continuity equation reflects the static-in-time divergence-free requirement on the velocity field. The flow is parameterized by the Reynolds number, which determines the ratio of inertial to viscous forces, $Re := \bar{u}h/\nu$, where $\bar{u}$ and h are the characteristic velocity and length of the flow and ν is the kinematic viscosity. Spatial coordinates in Equation 1 are nondimensionalized by h, velocity by $\bar{u}$, time by $h/\bar{u}$, and pressure by $\rho \bar{u}^2$, where ρ is the fluid density.

2.1. Mean Flow Equations

When the flow becomes turbulent, it reaches a statistically stationary state in which variables still vary in time but their statistics are time independent. To analyze the statistical properties of the flow, the velocity and pressure fields are decomposed into the sum of the turbulent mean components $(\bar{\mathbf{u}}, \bar{P})$ and fluctuations $(\mathbf{v}, p)$ around them:

$$(\mathbf{u}, P) = (\bar{\mathbf{u}} + \mathbf{v}, \bar{P} + p), \quad (\bar{\mathbf{u}}, \bar{P}) = (\langle \mathbf{u} \rangle, \langle P \rangle), \quad (\langle \mathbf{v} \rangle, \langle p \rangle) = (0, 0),$$

where $\langle \cdot \rangle$ denotes the time-average operator, e.g.,

$$\langle \mathbf{u}(\mathbf{x}, t) \rangle = \lim_{T \to \infty} \frac{1}{T} \int_0^T \mathbf{u}(\mathbf{x}, t + \tau) \, \mathrm{d}\tau.$$

Averaging Equation 1 yields the Reynolds-averaged NS equations (7, 39, 50)

$$\partial_t \bar{\mathbf{u}} + (\bar{\mathbf{u}} \cdot \nabla) \bar{\mathbf{u}} = -\nabla \bar{P} + \frac{1}{Re} \Delta \bar{\mathbf{u}} - \nabla \cdot \langle \mathbf{v} \mathbf{v}^T \rangle,$$
$$0 = \nabla \cdot \bar{\mathbf{u}}, \qquad \qquad 2.$$

which govern the evolution of the turbulent mean profiles $(\bar{\mathbf{u}}, \bar{P})$. Relative to Equation 1, Equation 2 contains one additional term that depends on the second-order moment of the velocity fluctuation vector $\mathbf{v}$, $\langle \mathbf{v} \mathbf{v}^T \rangle$. This symmetric tensor arises from momentum transfer by the velocity fluctuations and has a profound influence on the mean flow quantities and thereby on our ability to predict the skin-friction drag (39).

2.2. The Closure Problem

For a 3-D flow, Equation 2 consists of four independent equations governing the dynamics of the mean velocity and pressure fields $(\bar{\mathbf{u}}, \bar{P})$. However, these equations contain more than four unknowns; in addition to $\bar{\mathbf{u}}$ and $\bar{P}$, the Reynolds stresses $\langle \mathbf{v} \mathbf{v}^T \rangle$ are also unknown. This is a consequence of a closure problem that cannot be resolved in the absence of additional information about the second-order statistics of velocity fluctuations. Since the NS equations are nonlinear, the nth velocity moment depends on the $(n + 1)$th moment (39), making it challenging to determine such second-order statistics.

Statistical theories of turbulence attempt to overcome the closure problem by modeling the effect of the Reynolds stress tensor on the mean flow quantities rather than explicitly resolving the nonlinear terms (7, 39, 50). This is typically achieved by expressing higher-order moments in terms of the lower-order moments via a combination of physical intuition and empirical observations
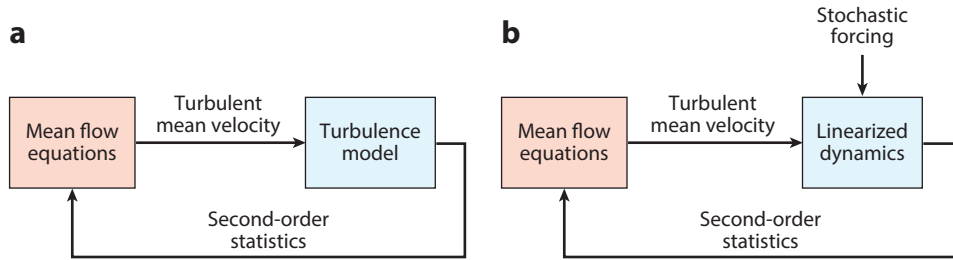
a

b

Stochastic forcing

Figure 1

(*a*) Conventional turbulence models are used to compute second-order statistics that drive the mean flow equations. (*b*) An alternative approach utilizes stochastically forced linearized dynamics around the turbulent mean velocity to compute the second-order statistics of velocity fluctuations.

with rigorous approximation of the flow equations (see **Figure 1*a***). For example, the turbulent viscosity hypothesis seeks approximate solutions of Equation 2 by relating turbulent stresses to mean velocity gradients via (50)

$$\langle \mathbf{v}\mathbf{v}^T \rangle - \frac{1}{3} \, \mathrm{trace}\left(\langle \mathbf{v}\mathbf{v}^T \rangle \right) I = -\frac{\nu_T}{Re}(\nabla\bar{\mathbf{u}} + (\nabla\bar{\mathbf{u}})^T),$$

where ν_T is the turbulent viscosity and I is the identity tensor. Unfortunately, a general-purpose expression for ν_T does not exist, and turbulence models are required to relate it to other flow quantities, e.g., second-order statistics of the velocity fluctuations.

With appropriate choices of velocity and length scales, turbulent viscosity can be expressed as (50)

$$\nu_T = cRe^2(k^2/\epsilon),$$

where k and ϵ denote the turbulent kinetic energy and its rate of dissipation, respectively, and c is the constant. The k-ϵ model (51, 52) provides two differential transport equations for computing k and ϵ and is widely used in commercial computational fluid dynamics codes and in engineering practice. Even though these equations are less complex than the NS equations, they are still computationally expensive, produce reliable results only for certain flow configurations, and are not convenient for control design and optimization (for additional details, see Reference 50). In what follows, we describe an alternative approach to turbulence modeling that approximates the Reynolds stresses using the second-order statistics of the stochastically forced NS equations linearized around the turbulent mean flow (see **Figure 1*b***). We also demonstrate how second-order statistics resulting from DNS and experiments can be used to refine the predictive capability of models that arise from first principles.

3. STOCHASTICALLY FORCED LINEARIZED NAVIER–STOKES EQUATIONS

The dynamics of small velocity and pressure fluctuations $(\mathbf{v}, p)$ around the turbulent mean profile $(\bar{\mathbf{u}}, \bar{P})$ are governed by the linearized NS and continuity equations

$$\partial_t \mathbf{v} + (\nabla \cdot \bar{\mathbf{u}})\mathbf{v} + (\nabla \cdot \mathbf{v})\bar{\mathbf{u}} = -\nabla p + \frac{1}{Re}\,\Delta\mathbf{v} + \mathbf{d},$$
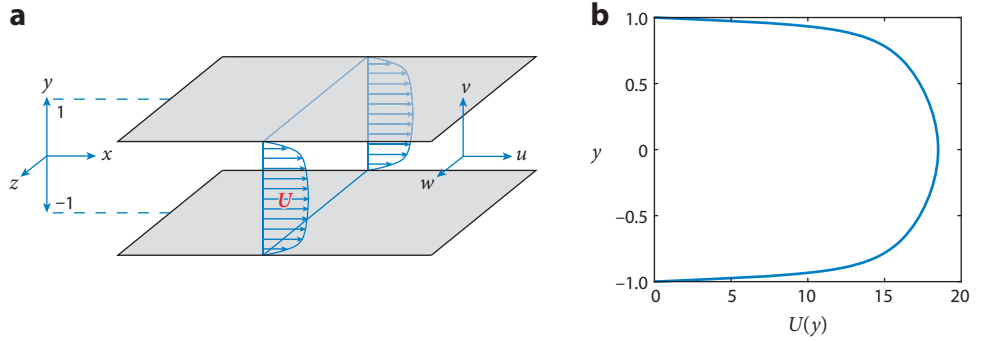$$0 = \nabla \cdot \mathbf{v}.$$

3.

Figure 2

(*a*) Geometry of a pressure-driven turbulent channel flow between two parallel infinite walls. (*b*) Turbulent mean velocity profile $U(y)$ in a flow with friction Reynolds number $Re = 186$.

Here, **d** represents an additive zero-mean stationary stochastic input that triggers a statistical response of the linearized dynamics. In what follows, we describe how available second-order statistics of turbulent channel flows can be reproduced using the stochastically forced model represented by Equation 3 and a suitable choice of power spectrum for the input **d**. While we focus on the turbulent channel flow, it is noteworthy that the reviewed methodology and theoretical framework are applicable to other flow configurations.

In strongly inertial regimes, all flows transition to turbulence, and a channel flow with the geometry shown in **Figure 2a** is commonly used as a benchmark for modeling, analysis, and control of wall-bounded turbulence. As illustrated in **Figure 2b**, the turbulent mean velocity in channel flow contains only a streamwise component $\bar{\mathbf{u}} = [U(y)\,0\,0]^T$, and the linearized model that governs the dynamics of velocity fluctuations $\mathbf{v} := [u\ v\ w]^T$ in the streamwise (x), wall-normal (y), and spanwise (z) directions takes the form

$$
\begin{aligned}
\partial_t u \ + \ U(y)\,\partial_x u \ + \ U'(y)\,v &= -\,\partial_x p + (1/Re)\,\Delta u + d_u, \\
\partial_t v \ + \ U(y)\,\partial_x v \qquad\quad &= -\,\partial_y p + (1/Re)\,\Delta v + d_v, \\
\partial_t w \ + \ U(y)\,\partial_x w \qquad\quad &= -\,\partial_z p + (1/Re)\,\Delta w + d_w, \\
0 &= \quad \partial_x u + \partial_y v + \partial_z w.
\end{aligned}
\qquad\qquad 4.
$$

Here, $U'(y) := dU(y)/dy$, and $\mathbf{d} := [d_u\ d_v\ d_w]^T$ is the body-forcing fluctuation vector. By selecting the channel half-height h and the friction velocity u_τ as the proper scales, the flow is characterized by the friction Reynolds number $Re := u_\tau h/\nu$.

The linearized dynamics in Equation 4 are time invariant and have constant coefficients in the wall-parallel directions; thus, the Fourier transform in x and z can be used to obtain a 1-D system of partial differential equations (in y and t) parameterized by the horizontal wavenumbers $\mathbf{k} := (k_x, k_z)$. Furthermore, a standard conversion can be used to eliminate the pressure from the equations and bring the descriptor form in Equation 4 into the form of an evolution model in which the state is determined by the wall-normal velocity (v) and vorticity ($\eta = \partial_z u - \partial_x w$) fluctuations (31, 53), with the boundary conditions $v(y = \pm 1, \mathbf{k}, t) = \partial_y v(y = \pm 1, \mathbf{k}, t) = \eta(y = \pm 1, \mathbf{k}, t) = 0.$[1] A pseudospectral technique (54) with N collocation points in y approximates the underlying operators, and a change of variables described in appendix A of Reference 55 is used to

---

[1]The evolution model is obtained from Equation 4 as follows. Applying the divergence operator ∇ to the linearized NS equations yields an expression for Δp. The equation for v is obtained by acting with the Laplacian

obtain a finite-dimensional state-space representation in which the energy of velocity fluctuations at any $\mathbf{k}$ is determined by the Euclidean norm of the state vector $\boldsymbol{\psi} := [v \; \eta]^T$:

$$\dot{\boldsymbol{\psi}}(\mathbf{k}, t) = A(\mathbf{k})\,\boldsymbol{\psi}(\mathbf{k}, t) + B(\mathbf{k})\,\mathbf{d}(\mathbf{k}, t),$$
$$\mathbf{v}(\mathbf{k}, t) = C(\mathbf{k})\,\boldsymbol{\psi}(\mathbf{k}, t). \qquad\qquad 5.$$

Here, $\boldsymbol{\psi}(\mathbf{k}, t) \in \mathbb{C}^{2N}$, $\mathbf{d}(\mathbf{k}, t) \in \mathbb{C}^{3N}$ is the input vector; $\mathbf{v}(\mathbf{k}, t) \in \mathbb{C}^{3N}$ is the velocity fluctuation vector; the matrix $A(\mathbf{k})$ determines dynamical interactions between the state variables; $B(\mathbf{k})$ specifies the way the input $\mathbf{d}(\mathbf{k}, t)$ enters into the evolution model; and the output matrix $C(\mathbf{k})$ relates the state vector $\boldsymbol{\psi}(\mathbf{k}, t)$ to the velocity fluctuation vector $\mathbf{v}(\mathbf{k}, t)$.

3.1. Algebraic Relations Between Input and State Statistics

In channel flow, the NS equations linearized around the turbulent mean flow are stable (56, 57), i.e., all eigenvalues of A in Equation 5 are in the left half of the complex plane, and the steady-state covariance matrix $X(\mathbf{k})$ of the state vector in Equation 5,

$$X(\mathbf{k}) = \lim_{t \to \infty} \mathbf{E}(\boldsymbol{\psi}(\mathbf{k}, t)\,\boldsymbol{\psi}^*(\mathbf{k}, t)), \qquad\qquad 6.$$

satisfies the Lyapunov-like equation (58, 59)

$$A(\mathbf{k})\,X(\mathbf{k}) + X(\mathbf{k})\,A^*(\mathbf{k}) = -B(\mathbf{k})\,H^*(\mathbf{k}) - H(\mathbf{k})\,B^*(\mathbf{k}), \qquad\qquad 7.$$

where $\mathbf{E}$ is the expectation operator and $*$ denotes the complex conjugate transpose. For colored-in-time $\mathbf{d}(\mathbf{k}, t)$, $H(\mathbf{k})$ is a matrix that quantifies the cross-correlation between the input and the state in Equation 5 in statistical steady state (appendix B of Reference 55):

$$H(\mathbf{k}) = \lim_{t \to \infty} \mathbf{E}(\boldsymbol{\psi}(\mathbf{k}, t)\mathbf{d}^*(\mathbf{k}, t)) + \frac{1}{2}B(\mathbf{k})\,\Omega(\mathbf{k}).$$

When the input $\mathbf{d}(\mathbf{k}, t)$ in Equation 5 is zero-mean and white-in-time with covariance matrix $\Omega(\mathbf{k})$, i.e., $\mathbf{E}(\mathbf{d}(\mathbf{k}, t)) = 0$ and $\mathbf{E}(\mathbf{d}(\mathbf{k}, t)\,\mathbf{d}^*(\mathbf{k}, \tau)) = \Omega(\mathbf{k})\delta(t - \tau)$, the matrix $H(\mathbf{k})$ simplifies to $H(\mathbf{k}) = (1/2)B(\mathbf{k})\Omega(\mathbf{k})$, and Equation 7 reduces to the standard algebraic Lyapunov equation

$$A(\mathbf{k})\,X(\mathbf{k}) + X(\mathbf{k})\,A^*(\mathbf{k}) = -B(\mathbf{k})\Omega(\mathbf{k})B^*(\mathbf{k}). \qquad\qquad 8.$$

The steady-state velocity covariance matrix $V(\mathbf{k})$ can be obtained from $X(\mathbf{k})$:

$$V(\mathbf{k}) = \lim_{t \to \infty} \mathbf{E}(\mathbf{v}(\mathbf{k}, t)\,\mathbf{v}^*(\mathbf{k}, t)) = C(\mathbf{k})\,X(\mathbf{k})\,C^*(\mathbf{k}). \qquad\qquad 9.$$

Since the dynamics are parameterized by wavenumbers $\mathbf{k}$, the entries of $V(\mathbf{k})$ determine two-point correlations of velocity fluctuations in the wall-normal direction y (see Reference 60).

3.2. Spatiotemporal Correlations

At any $\mathbf{k}$, the matrix $V(\mathbf{k})$ determines two-point correlations in the wall-normal direction of velocity fluctuations in statistical steady state, and the lagged covariance matrix

$$R_{\mathbf{vv}}(\mathbf{k}, \tau) := \lim_{t \to \infty} \mathbf{E}(\mathbf{v}(\mathbf{k}, t)\,\mathbf{v}^*(\mathbf{k}, t + \tau)) \qquad\qquad 10.$$

Δ on the second equation in Equation 4 and utilizing the expression for Δp to eliminate the pressure p. The equation for η is obtained by taking the curl of the linearized NS equations. This yields two partial differential equations that govern the evolution of v and η and involve only v, η, and $\mathbf{d}$.

captures spatiotemporal correlations. Furthermore, the application of the temporal Fourier transform yields the spectral density matrix $S_{\mathbf{vv}}(\mathbf{k}, \omega)$ of the output $\mathbf{v}(\mathbf{k}, t)$,

$$S_{\mathbf{vv}}(\mathbf{k}, \omega) = \int_{-\infty}^{+\infty} R_{\mathbf{vv}}(\mathbf{k}, \tau)\, e^{-i\omega\tau}\, d\tau, \tag{11.}$$

which parameterizes two-point velocity correlations across wavenumbers $\mathbf{k}$ and temporal frequencies ω. The matrix $S_{\mathbf{vv}}(\mathbf{k}, \omega)$ can be expressed in terms of the spectral density matrix $S_{\mathbf{dd}}(\mathbf{k}, \omega)$ of the input $\mathbf{d}(\mathbf{k}, t)$:

$$S_{\mathbf{vv}}(\mathbf{k}, \omega) = T_{\mathbf{vd}}(\mathbf{k}, \omega)\, S_{\mathbf{dd}}(\mathbf{k}, \omega)\, T_{\mathbf{vd}}^{*}(\mathbf{k}, \omega),$$

where $T_{\mathbf{vd}}(\mathbf{k}, \omega)$ is the spatiotemporal frequency response of the linear time-invariant (LTI) system in Equation 5,

$$\mathbf{v}(\mathbf{k}, \omega) = T_{\mathbf{vd}}(\mathbf{k}, \omega)\, \mathbf{d}(\mathbf{k}, \omega) = C(\mathbf{k})(i\omega I - A(\mathbf{k}))^{-1} B(\mathbf{k})\, \mathbf{d}(\mathbf{k}, \omega). \tag{12.}$$

The steady-state output covariance matrix $V(\mathbf{k})$ is related to the spectral density matrix $S_{\mathbf{vv}}(\mathbf{k}, \omega)$ via

$$V(\mathbf{k}) := R_{\mathbf{vv}}(\mathbf{k}, 0) = \frac{1}{2\pi} \int_{-\infty}^{+\infty} S_{\mathbf{vv}}(\mathbf{k}, \omega)\, d\omega. \tag{13.}$$

Finally, for white-in-time input $\mathbf{d}(\mathbf{k}, t)$ in Equation 5, the lagged output covariance matrix $R_{\mathbf{vv}}(\mathbf{k}, \tau)$ can be expressed as a linear function of the steady-state covariance matrix $X(\mathbf{k})$:

$$R_{\mathbf{vv}}(\mathbf{k}, \tau) = C(\mathbf{k})X(\mathbf{k})\, e^{A^{*}(\mathbf{k})\tau} C^{*}(\mathbf{k}). \tag{14.}$$

3.3. Summary

For the LTI dynamics in Equation 5, the algebraic constraint in Equation 7 determines admissible steady-state covariance matrices $X(\mathbf{k})$. Among all positive semidefinite matrices, this constraint identifies those that qualify as state covariances for a state-space representation with matrices $A(\mathbf{k})$ and $B(\mathbf{k})$. As shown by Georgiou (58, 59), the structure of state covariances is an inherent property of the linear dynamics. The sidebar titled Admissible Covariances describes necessary and sufficient conditions for a positive-definite matrix $X(\mathbf{k})$ to qualify as a steady covariance matrix of

---

ADMISSIBLE COVARIANCES

The matrix $X = X^{*} \succ 0$ is the stationary covariance matrix of the state of the LTI system in Equation 5 with controllable pair (A, B) and suitable input process $\mathbf{d}$ if and only if

$$\operatorname{rank} \begin{bmatrix} AX + XA^{*} & B \\ B^{*} & 0 \end{bmatrix} = \operatorname{rank} \begin{bmatrix} 0 & B \\ B^{*} & 0 \end{bmatrix}$$

or, equivalently, if and only if the matrix equation

$$BH^{*} + HB^{*} = -(AX + XA^{*})$$

has a solution H (58, 59). The rank condition implies that any positive-definite matrix X is admissible as a stationary covariance of the state of an LTI system if the input matrix B is full row rank.
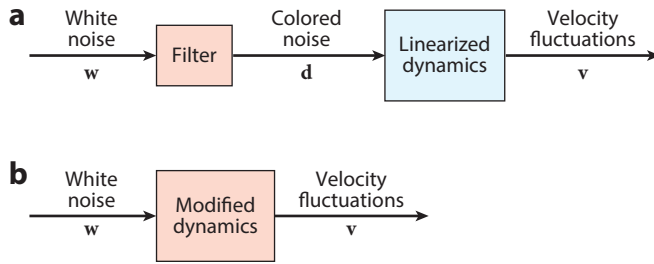
Figure 3

(*a*) The cascade connection of the linearized dynamics with a spatiotemporal linear filter that is designed to account for partially available second-order statistics of turbulent channel flow. (*b*) An equivalent reduced-order representation of the cascade connection in panel *a*. Figure adapted from Reference 55 with permission.

the state $\boldsymbol{\psi}(\mathbf{k}, t)$ in Equation 5. These conditions amount to the solvability of Equation 7 for the matrix $H(\mathbf{k})$ or, equivalently, the rank condition in the sidebar. We next build on such structural constraints on admissible covariances and formulate convex optimization problems for characterizing the statistical properties of stochastic excitations to LTI systems that account for partially available statistics in turbulent channel flow.

4. COMPLETION OF PARTIALLY AVAILABLE FLOW STATISTICS

The algebraic relations described in Section 3.1 can be used to compute the steady covariance matrix $X(\mathbf{k})$ of the stochastically forced LTI system in Equation 5 based on the linearized model [i.e., the matrices $A(\mathbf{k})$ and $B(\mathbf{k})$] and the input statistics. In stochastic dynamic modeling of turbulent flows, however, the converse is of interest: Starting from the covariance matrix $X(\mathbf{k})$ and the dynamic matrix $A(\mathbf{k})$ in Equation 5, the objective is to identify the directionality of the disturbance [i.e., the matrix $B(\mathbf{k})$ in Equation 5] and the power spectrum of the stochastic input $\mathbf{d}(\mathbf{k}, t)$ that generate such state statistics. As illustrated in **Figure 3a**, this amounts to designing a linear filter that is driven by white noise and produces input $\mathbf{d}(\mathbf{k}, t)$ that generates the desired covariance matrix $X(\mathbf{k})$ for the LTI system in Equation 5. In high-Reynolds-number flows, experimental and computational limitations often lead to only partial knowledge of flow statistics. For example, in experiments, an array of probes may provide only a limited subset of spatiotemporal correlations for velocity fluctuations, and in numerical simulations, certain regions of the computational domain may be poorly resolved. In this section, we formulate the problem of completing partially known state correlations in a way that is consistent with the hypothesis that perturbations around the turbulent mean velocity are generated by the linearized NS equations. To accomplish this objective, we seek stochastic forcing models of low complexity, where complexity is quantified by the number of degrees of freedom that are directly influenced by stochastic forcing in the linearized evolution model.

4.1. The Necessity of Colored-in-Time Stochastic Forcing

The right-hand side of the standard algebraic Lyapunov equation shown in Equation 8 is sign definite, i.e., $B(\mathbf{k}) \, \Omega(\mathbf{k}) B^*(\mathbf{k}) \succeq 0$. By contrast, the right-hand side of the Lyapunov-like equation shown in Equation 7 is in general sign indefinite, and unless the input $\mathbf{d}(\mathbf{k}, t)$ in Equation 5 is
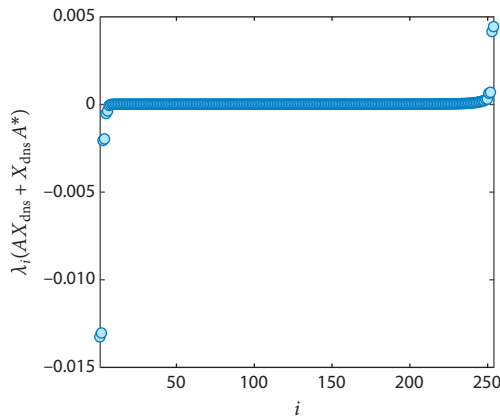
Figure 4

Positive eigenvalues of the matrix $A(\mathbf{k})X_{\mathrm{dns}}(\mathbf{k}) + X_{\mathrm{dns}}(\mathbf{k})A^*(\mathbf{k})$ for channel flow with $Re = 186$ and $\mathbf{k} = (2.5, 7)$, indicating that turbulent velocity covariances cannot be reproduced by the linearized Navier–Stokes equations with white-in-time stochastic forcing (see Equation 8). Figure adapted from Reference 55 with permission.

white-in-time, the matrix

$$Z(\mathbf{k}) := -(A(\mathbf{k})X(\mathbf{k}) + X(\mathbf{k})A^*(\mathbf{k})) = B(\mathbf{k})H^*(\mathbf{k}) + H(\mathbf{k})B^*(\mathbf{k}) \qquad 15.$$

can have both positive and negative eigenvalues. **Figure 4** shows the eigenvalues of the matrix $A(\mathbf{k})X_{\mathrm{dns}}(\mathbf{k}) + X_{\mathrm{dns}}(\mathbf{k})A^*(\mathbf{k})$ for a channel flow with $Re = 186$ and $\mathbf{k} = (2.5, 7)$, where $A(\mathbf{k})$ denotes the generator of the dynamics in Equation 5 obtained by linearization around the turbulent mean velocity profile and $X_{\mathrm{dns}}(\mathbf{k})$ is the steady-state covariance matrix resulting from numerical simulations of the nonlinear NS equations. The presence of both positive and negative eigenvalues indicates that the second-order statistics of turbulent channel flow cannot be reproduced by the linearized NS equations with white-in-time stochastic excitation. The modeling and optimization framework that was recently developed by Zare et al. (55, 61) overcomes this limitation by departing from the white-in-time restriction on stochastic forcing.

4.2. Covariance Completion via Convex Optimization

For the dynamical generator A resulting from linearization of the NS equations around the turbulent mean velocity, the steady-state covariance matrix X satisfies

$$AX + XA^* + Z = 0, \qquad 16a.$$

where

$$Z := BH^* + HB^* \qquad 16b.$$

quantifies the contribution of stochastic excitation. For notational convenience, we omit the dependence on the wavenumber $\mathbf{k}$ in this section. We assume that a subset of entries of the output covariance matrix V, namely V_{ij} for a selection of indices $(i, j) \in \mathcal{I}$, is available. This yields an additional set of linear constraints for the matrix X:

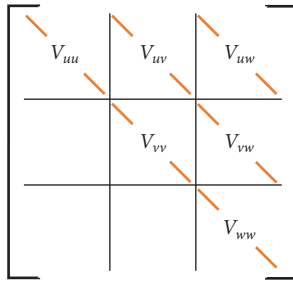$$(CXC^*)_{ij} = V_{ij}, \quad (i, j) \in \mathcal{I}. \qquad 16c.$$

Figure 5

Structure of the output covariance matrix V. The available one-point correlations of the velocity vector **v** in the wall-normal direction at various wavenumbers **k** are marked by the orange lines. Figure adapted from Reference 55 with permission.

For example, such known entries may represent one-point correlations in the wall-normal direction (see **Figure 5**). At any **k**, the diagonals of the submatrices $V_{uu}(\mathbf{k})$, $V_{vv}(\mathbf{k})$, and $V_{ww}(\mathbf{k})$ denote the normal Reynolds stresses in turbulent channel flow, e.g.,

$$\mathrm{diag}(V_{uu}(\mathbf{k})) = \mathrm{diag}\left(\lim_{t \to \infty} \mathbf{E}(u(\mathbf{k},t)\, u^*(\mathbf{k},t))\right),$$

and the main diagonal of the submatrices $V_{uv}(\mathbf{k})$, $V_{uw}(\mathbf{k})$, and $V_{vw}(\mathbf{k})$ denote the shear stresses, e.g., $\mathrm{diag}(V_{uv}(\mathbf{k})) = \mathrm{diag}(\lim_{t \to \infty} \mathbf{E}(u(\mathbf{k},t)\, v^*(\mathbf{k},t)))$.[2] It is noteworthy that while the covariance matrix X is not allowed to have negative eigenvalues, the matrix Z can be sign indefinite. Our objective is to identify suitable choices of X and Z that satisfy the above constraints and yield a low-complexity model for the stochastic input that explains the observed statistics.

The contribution of the stochastic excitation enters through the matrix Z, which is of the form given by Equation 16b, where the directionality of the input and its time correlations are reflected by the choices of matrices B and H. As discussed in the sidebar titled Admissible Covariances, when the input matrix B is full rank, any positive semidefinite X qualifies as the steady-state covariance of the stochastically forced linearized NS equation shown as Equation 5. However, as demonstrated by Zare et al. (55), in this case a forcing model that cancels the linearized dynamics and obscures important aspects of the underlying physics becomes a viable option. It is thus important to minimize the number of degrees of freedom that can be directly influenced by stochastic forcing. This minimization can be accomplished via suitable regularization, e.g., by minimizing the rank of the matrix Z in Equation 16a (61, 62).[3]

This regularization gives rise to the following optimization problem, where the objective function provides a trade-off between the solution to the maximum-entropy problem and the complexity of the forcing model, and the positive regularization parameter γ reflects the relative weight of the nuclear norm objective. The convexity of the optimization problem follows from the convexity of its objective function and the linearity of its constraint set, thereby implying the existence of a globally optimal minimizer.

Problem 1 (covariance completion problem). Given matrices A and C, the available entries V_{ij} of the output covariance matrix V, and the positive regularization parameter γ,

---

[2]In statistical steady state, turbulent kinetic energy is determined by the sum of traces of matrices V_{uu}, V_{vv}, and V_{ww}, and skin-friction drag depends on the shear stress $\mathrm{diag}(V_{uv})$.

[3]The rank of the matrix Z bounds the number of independent input channels or columns in matrix B; for details, see Reference 61.

determine the Hermitian matrices X and Z that solve the convex optimization problem

$$
\begin{aligned}
\underset{X, Z}{\text{minimize}} \quad & -\log \det(X) + \gamma \, \|Z\|_{\star} \\
\text{subject to} \quad & AX + XA^* + Z = 0, \\
& (CXC^*)_{ij} = V_{ij}, \ (i, j) \in \mathcal{I}.
\end{aligned}
\tag{17.}
$$

The first constraint reflects the requirement that the second-order statistics be consistent with a stochastically forced linearized model, and the second constraint requires that the available elements of the matrix V be exactly reproduced. Minimizing the logarithmic barrier function ensures the positive definiteness of the covariance matrix X (63) and results in a maximum-entropy stochastic realization (64). On the other hand, the nuclear norm regularizer—i.e., the sum of singular values of the matrix Z, $\|Z\|_{\star} = \sum_i \sigma_i(Z)$—is introduced to restrict the rank of Z (65, 66) and thereby reduce the complexity of the forcing model.

4.2.1. Power spectrum of stochastic input and filter design. The solution of the covariance completion problem—i.e., the Hermitian matrices $X(\mathbf{k})$ and $Z(\mathbf{k})$—can be used to obtain a dynamical model for colored-in-time stochastic input to the linearized NS equations. Zare et al. (55, 61) recently developed a class of generically minimal linear filters that have the same number of degrees of freedom as the finite-dimensional approximation of the linearized model.

Since channel flow is translationally invariant in the wall-parallel dimensions, the dynamics in Equation 5 and the optimization problem in Equation 17 are decoupled over the wavenumbers $\mathbf{k} = (k_x, k_z)$. At each $\mathbf{k}$, the filter dynamics that account for $X(\mathbf{k})$ are given by

$$
\begin{aligned}
\dot{\boldsymbol{\phi}}(\mathbf{k}, t) &= (A(\mathbf{k}) - B(\mathbf{k})K(\mathbf{k})) \, \boldsymbol{\phi}(\mathbf{k}, t) + B(\mathbf{k}) \, \mathbf{w}(\mathbf{k}, t), \\
\mathbf{d}(\mathbf{k}, t) &= -K(\mathbf{k}) \, \boldsymbol{\phi}(\mathbf{k}, t) + \mathbf{w}(\mathbf{k}, t),
\end{aligned}
\tag{18.}
$$

where $\boldsymbol{\phi}(\mathbf{k}, t)$ is the state of the filter and $\mathbf{w}(\mathbf{k}, t)$ is a zero-mean white-in-time stochastic process with covariance $\Omega(\mathbf{k})$. On the other hand,

$$
K(\mathbf{k}) = \left(\frac{1}{2} \Omega(\mathbf{k}) B^*(\mathbf{k}) - H^*(\mathbf{k}) \right) X^{-1}(\mathbf{k})
\tag{19.}
$$

for matrices $B(\mathbf{k})$ and $H(\mathbf{k})$ that correspond to the factorization $Z(\mathbf{k}) = B(\mathbf{k})H^*(\mathbf{k}) + H(\mathbf{k})B^*(\mathbf{k})$ (for details, see Reference 61). The linear filter represented by Equation 18 generates a colored-in-time stochastic input $\mathbf{d}(\mathbf{k}, t)$ to the linearized NS equations shown in Equation 5, and the resulting cascade connection reproduces the available second-order statistics of turbulent flow (see **Figure 3a**). The spectral density of $\mathbf{d}(\mathbf{k}, t)$,

$$
S_{\mathbf{dd}}(\mathbf{k}, \omega) = T_{\mathbf{dw}}(\mathbf{k}, \omega) \, \Omega(\mathbf{k}) \, T_{\mathbf{dw}}^*(\mathbf{k}, \omega),
$$

determines the spectral content of the input to the LTI system, where

$$
T_{\mathbf{dw}}(\mathbf{k}, \omega) = -K(\mathbf{k})(\mathrm{i}\omega I - A(\mathbf{k}) + B(\mathbf{k})K(\mathbf{k}))^{-1} B(\mathbf{k}) + I
$$

is the spatiotemporal frequency response of the linear filter in Equation 18.

4.2.2. Minimal realization. The state-space representation corresponding to the cascade connection of the linear filter in Equation 18 with the linearized NS dynamics in Equation 5 is given by

$$\begin{bmatrix} \dot{\boldsymbol{\psi}}(\mathbf{k},t) \\ \dot{\boldsymbol{\phi}}(\mathbf{k},t) \end{bmatrix} = \begin{bmatrix} A(\mathbf{k}) & -B(\mathbf{k})K(\mathbf{k}) \\ 0 & A(\mathbf{k}) - B(\mathbf{k})K(\mathbf{k}) \end{bmatrix} \begin{bmatrix} \boldsymbol{\psi}(\mathbf{k},t) \\ \boldsymbol{\phi}(\mathbf{k},t) \end{bmatrix} + \begin{bmatrix} B(\mathbf{k}) \\ B(\mathbf{k}) \end{bmatrix} \mathbf{w}(\mathbf{k},t),$$

$$\mathbf{v}(\mathbf{k},t) = [C(\mathbf{k}) \quad 0] \begin{bmatrix} \boldsymbol{\psi}(\mathbf{k},t) \\ \boldsymbol{\phi}(\mathbf{k},t) \end{bmatrix}. \qquad 20.$$

This realization has twice as many states as the spatial discretization of the linearized NS model in Equation 5 but is not controllable and therefore not minimal. As shown by Zare et al. (61), removal of the uncontrollable states yields the minimal realization of the mapping from the input $\mathbf{w}(\mathbf{k}, \omega)$ to the output $\mathbf{v}(\mathbf{k}, \omega)$, $\mathbf{v}(\mathbf{k}, \omega) = T_{\mathbf{vw}}(\mathbf{k}, \omega)\mathbf{w}(\mathbf{k}, \omega)$,

$$T_{\mathbf{vw}}(\mathbf{k}, \omega) = C(\mathbf{k})\left(i\omega I - A(\mathbf{k}) + B(\mathbf{k})K(\mathbf{k})\right)^{-1}B(\mathbf{k}), \qquad 21.$$

as

$$\dot{\boldsymbol{\psi}}(\mathbf{k},t) = (A(\mathbf{k}) - B(\mathbf{k})K(\mathbf{k}))\boldsymbol{\psi}(\mathbf{k},t) + B(\mathbf{k})\,\mathbf{w}(\mathbf{k},t),$$
$$\mathbf{v}(\mathbf{k},t) = C(\mathbf{k})\,\boldsymbol{\psi}(\mathbf{k},t). \qquad 22.$$

This system has the same number of degrees of freedom as the system in Equation 5, and the corresponding algebraic Lyapunov equation in conjunction with Equation 19 yields

$$(A(\mathbf{k}) - B(\mathbf{k})K(\mathbf{k}))X(\mathbf{k}) + X(\mathbf{k})(A(\mathbf{k}) - B(\mathbf{k})K(\mathbf{k}))^* + B(\mathbf{k})\,\Omega(\mathbf{k})\,B^*(\mathbf{k})$$
$$= A(\mathbf{k})X(\mathbf{k}) + X(\mathbf{k})A^*(\mathbf{k}) + B(\mathbf{k})\,\Omega(\mathbf{k})\,B^*(\mathbf{k}) - B(\mathbf{k})K(\mathbf{k})X(\mathbf{k}) - X(\mathbf{k})K^*(\mathbf{k})B^*(\mathbf{k})$$
$$= A(\mathbf{k})X(\mathbf{k}) + X(\mathbf{k})A^*(\mathbf{k}) + B(\mathbf{k})\,H^*(\mathbf{k}) + H(\mathbf{k})\,B^*(\mathbf{k}) = 0.$$

This demonstrates that the state-space realization in Equation 18 generates a stochastic input $\mathbf{d}(\mathbf{k}, t)$, which is consistent with the steady-state covariance matrix $X(\mathbf{k})$.

> **Remark 1.** From Equation 19, we have $H(\mathbf{k}) = \frac{1}{2}B(\mathbf{k})\Omega(\mathbf{k}) - X(\mathbf{k})K^*(\mathbf{k})$, and substitution of this expression into Equation 7 yields the standard algebraic Lyapunov equation
>
> $$(A(\mathbf{k}) - B(\mathbf{k})K(\mathbf{k}))X(\mathbf{k}) + X(\mathbf{k})(A(\mathbf{k}) - B(\mathbf{k})K(\mathbf{k}))^* = -B(\mathbf{k})\,\Omega(\mathbf{k})B^*(\mathbf{k}).$$

Since the pair $(A(\mathbf{k}), B(\mathbf{k}))$ is controllable, so are $(A(\mathbf{k}) - B(\mathbf{k})K(\mathbf{k}), B(\mathbf{k}))$ and $(A(\mathbf{k}) - B(\mathbf{k})K(\mathbf{k}), B(\mathbf{k})\Omega^{1/2}(\mathbf{k}))$. The stability of the modified dynamical generator $A(\mathbf{k}) - B(\mathbf{k})K(\mathbf{k})$ follows from the positive semidefiniteness of $B(\mathbf{k})\,\Omega(\mathbf{k})B^*(\mathbf{k})$ via standard Lyapunov theory.

The minimal realization (given by Equation 22) of the cascade connection described by Equation 20 is advantageous from a computational standpoint and allows for an alternative interpretation of the stochastic realization of colored-in-time forcing. First, time-domain simulations require numerical integration of the system in Equation 22, which has half the number of states of the system in Equation 20, thereby offering a computational speedup. On the other hand, the structure in Equation 22 suggests that the colored-in-time forcing realized by the LTI filter in Equation 18 can be equivalently interpreted as a white-in-time excitation together with a dynamical modification to the linearized equations in the form of state-feedback interactions
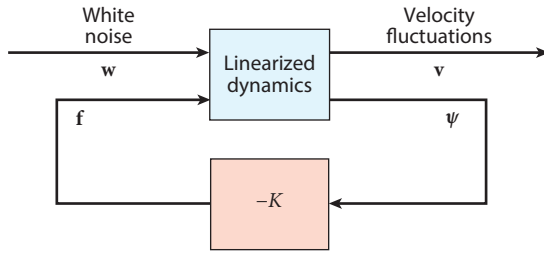
Figure 6

A feedback connection of the linearized dynamics with a static gain matrix K that is designed to account for the sampled steady-state covariance matrix X.

(see **Figure 3b**). This interpretation provides an alternative viewpoint that is closely related to a class of stochastic control (67–70) and output covariance estimation (71, 72) problems (for details, see section II.C of Reference 61). Based on this viewpoint, we next describe an alternative formulation of the covariance completion problem as a state-feedback synthesis that is optimal with respect to a different design criterion (73, 74).

4.3. Minimum-Control-Energy Covariance Completion

As described by Zare et al. (73, 74), the challenge of establishing consistency between statistical measurements and a linearized model can be alternatively cast as the problem of seeking a completion of the missing entries of a covariance matrix X along with a perturbation Δ of the system dynamics subject to white-in-time input $\mathbf{w}$:

$$\dot{\boldsymbol{\psi}} = (A + \Delta)\,\boldsymbol{\psi} + \mathbf{w},$$
$$\mathbf{v} = C\,\boldsymbol{\psi}.$$

For $\Delta := -BK$, a covariance completion problem can be formulated as an optimal control problem aimed at designing a stabilizing state-feedback control law $\mathbf{f} = -K\boldsymbol{\psi}$ (**Figure 6**). The choice of B may incorporate added insights into the strength and directionality of possible couplings between state variables. While a full-rank matrix B that allows the perturbation signal $K\boldsymbol{\psi}$ to manipulate all degrees of freedom can lead to the complete cancellation of the original dynamics A, it is also important to impose a penalty on the average quadratic size of signals $K\boldsymbol{\psi}$. This gives rise to the following convex optimization problem, where the objective function provides a trade-off between the minimum-control-energy problem and the number of feedback couplings that need to be introduced to modify the dynamical generator A and achieve consistency with available data (73, 74).

Problem 2 (minimum-energy covariance completion problem). Given matrices A, B, C, R, and Ω; the available entries V_{ij} of the output covariance matrix V; and the positive regularization parameter γ, determine the matrices K and X that solve convex optimization problem

$$\begin{aligned}
&\underset{K,X}{\text{minimize}}\ \ \text{trace}\,(K^* R K X) + \gamma \sum_{i=1}^{n} w_i \|e_i^* K\|_2 \\
&\text{subject to}\ \ (A - BK)X + X(A - BK)^* + \Omega = 0, \\
&\qquad\qquad\quad (CXC^*)_{ij} = V_{ij},\ \ (i,j) \in \mathcal{I}, \\
&\qquad\qquad\quad X \succ 0.
\end{aligned} \qquad\qquad 23.$$

The algebraic constraint on K and X ensures closed-loop stability (see Remark 1) and consistency with the state covariance matrix X, and the second equality constraint requires that the available elements of the matrix V be exactly reproduced. The positive-definite matrix R specifies a penalty on the control input, while the weighted-norm regularizer promotes sparsity on the rows of the matrix K. Here, w_i are given positive weights, e$_i$ is the ith unit vector in $\mathbb{R}^m$, and $\Omega \succeq 0$ is the covariance matrix of white noise input **w**.

Remark 2. As demonstrated by Zare et al. (61, 74, 75), the covariance completion problems represented by Equations 17 and 23 can be cast as semidefinite programs. Small- and medium-size problems can be solved efficiently using standard solvers (63, 76, 77). To deal with the large problem dimensions that arise in fluid dynamics, Zare et al. (61, 74) have developed customized algorithms.

4.4. Completion of Spatiotemporal Correlations

The covariance matrix $V(\mathbf{k})$ provides information about spatial correlations of velocity fluctuations in statistical steady state. As described in Section 3.2, the temporal dependence of such statistics is captured by the spectral density matrix $S_{\mathbf{vv}}(\mathbf{k}, \omega)$. This matrix can be used to provide real-time estimates of the flow state (78), and recent efforts have been directed at estimating $S_{\mathbf{vv}}(\mathbf{k}, \omega)$ by matching individual entries at either specified temporal frequencies (79–81) or the spectral power (82), trace($S_{\mathbf{vv}}(\mathbf{k}, \omega)$). Either way, it should be independently considered whether the colored-in-time forcing models constructed in this way preserve important aspects of the original linearized NS dynamics. For additional discussion on parsimonious models and how these may reflect underlying physics, see Section 4.2.

5. CASE STUDY: TURBULENCE MODELING IN CHANNEL FLOW

In this section, we investigate the completion of partially known second-order statistics of a turbulent channel flow using the framework presented in Section 4.2. The mean velocity profile and one-point velocity correlations in the wall-normal direction at various wavenumber pairs **k** are obtained from DNS of a turbulent channel flow with friction Reynolds number $Re = 186$ (53, 83–85) (see **Figures 2b** and **5**). We also show how the modified dynamics of Section 4.2.1 can be used as a low-dimensional model that is simulated in time to generate velocity fluctuations whose second-order statistics are consistent with numerical simulations of the nonlinear NS equations.

5.1. Reproducing Available and Completing Unavailable Second-Order Statistics

As demonstrated by Zare et al. (55), Problem 1 is feasible at all wavenumbers **k**. Thus, regardless of the value of the regularization parameter γ, all available one-point correlations of turbulent channel flow can be reproduced by a stochastically forced linearized model. **Figure 7** displays perfect matching of all one-point velocity correlations that result from integration over wall-parallel wavenumbers. Since Problem 1 is not feasible for $Z(\mathbf{k}) \succeq 0$ at all **k**, this cannot be achieved with white-in-time stochastic forcing.

In addition to matching available one-point correlations, we next demonstrate that the solution to Problem 1 provides good recovery of two-point correlations. These are not used as problem data in the covariance completion problem and correspond to off-diagonal entries in **Figure 5**. While the diagonal entries of V determine the kinetic energy and affect the mean momentum
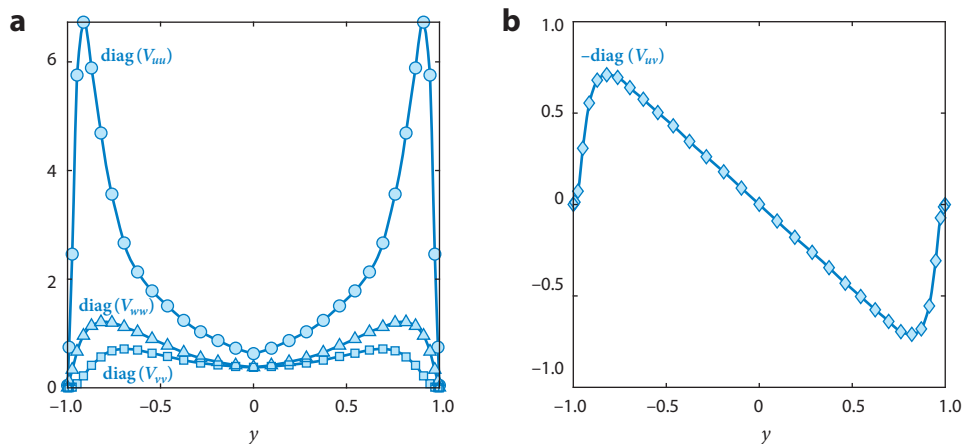
Figure 7

Correlation profiles of (*a*) normal and (*b*) shear stresses resulting from direct numerical simulation of turbulent channel flow with $Re = 186$ (*lines*) and from the solution to Problem 1: diag(V_{uu}) (*circles*), diag(V_{vv}) (*squares*), diag(V_{ww}) (*triangles*), and $-$diag(V_{uv}) (*diamonds*). Profiles are integrated over the wall-parallel wavenumbers $\mathbf{k}$. Figure adapted from Reference 55 with permission.

transfer in the turbulent flow, the off-diagonal two-point correlations are indicators of coherent flow structures that reside at various locations away from the wall (11, 86). The premultiplied energy spectrum in channel flow with $Re = 186$ peaks at $\mathbf{k} = (2.5, 7)$ (e.g., see figure 12*a* in Reference 87). **Figures 8*a*** and **8*c*** display, respectively, the streamwise V_{uu} and streamwise/wall-normal V_{uv} covariance matrices resulting from DNS at these flow conditions; **Figures 8*b*** and **8*d*** show the same covariance matrices that are obtained from the solution to Problem 1 (for a detailed examination of wall-normal and spanwise covariance matrices, see Reference 55). The quality of recovery depends on the choice of the regularization parameter γ, and for $\gamma = 300$, approximately 60% of the DNS-generated covariance matrix V_{dns} can be recovered based on a relative Frobenius norm measure, $\|V - V_{\mathrm{dns}}\|_F / \|V_{\mathrm{dns}}\|_F$. Here, $V = CXC^*$ represents the two-point correlation matrix of velocity fluctuations resulting from Problem 1. The high-quality recovery of two-point correlations is attributed to the structural constraint in Equation 16a, which keeps physics in the mix and enforces consistency between data and the linearized NS dynamics.

5.2. Stochastic Linear Simulations

Stochastic simulations of the modified LTI dynamics in Equation 22 can be used to verify the theoretical predictions resulting from the modeling and optimization framework of Section 4.2. For a spatial discretization with $N = 127$ collocation points in the wall-normal direction, at each wavenumber $\mathbf{k}$, the LTI system in Equation 22 has 254 states. For $\mathbf{k} = (2.5, 7)$ and $\gamma = 10^4$, the matrix Z that solves Problem 1 has eight nonzero eigenvalues (six positive and two negative) (see **Figure 9*a***). As shown by Zare et al. (61), the maximum number of positive or negative eigenvalues of the matrix Z bounds the number of inputs into the linearized NS model given by Equation 5. This implies that partially available statistics can be reproduced with six colored-in-time inputs, and as a result, the dynamical modification BK in Equation 22 is of rank 6.

Proper comparison with DNS or experiments requires ensemble averaging, rather than comparison at the level of individual stochastic simulations. To this end, we conducted 20 simulations with different realizations of white-in-time input $\mathbf{w}(\mathbf{k}, t)$ in Equation 22. The total simulation time was 400 viscous time units. **Figure 9*b*** shows the time evolution of the energy (variance) of
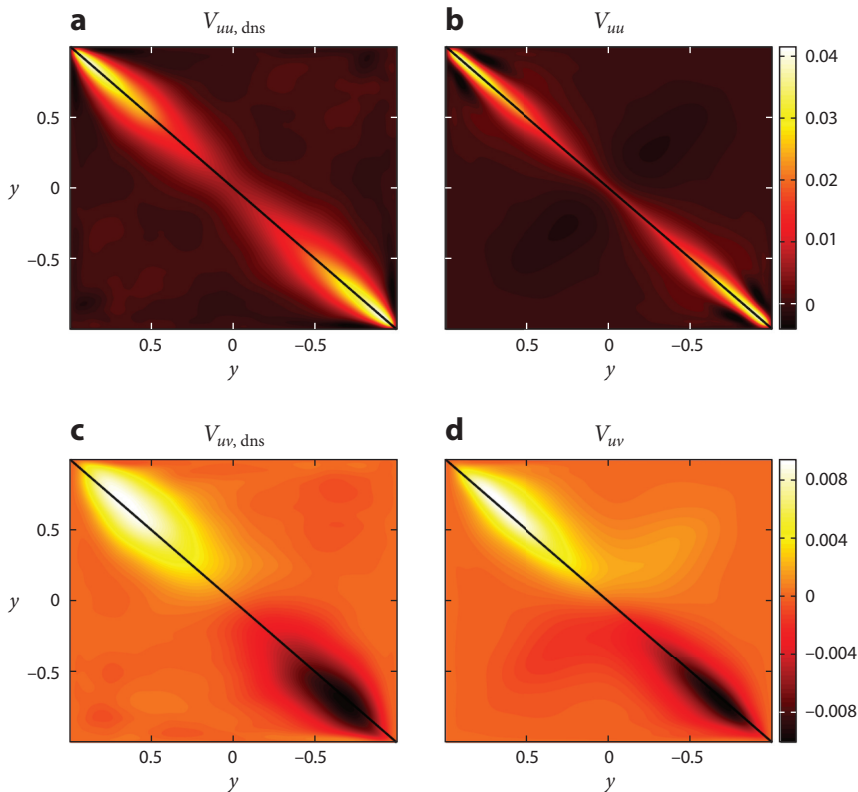
Figure 8

Covariance matrices resulting from (*a,c*) direct numerical simulation of turbulent channel flow with $Re = 186$ and (*b,d*) the solution to Problem 1 with $\gamma = 300$. Panels *a* and *b* show streamwise V_{uu} covariance matrices for $\mathbf{k} = (2.5, 7)$; panels *c* and *d* show streamwise/wall-normal V_{uv} covariance matrices for the same $\mathbf{k}$. The one-point correlation profiles that are used as data in Problem 1 are marked by black lines along the main diagonals. Figure adapted from Reference 55 with permission.

velocity fluctuations resulting from these 20 simulations. Even though the responses of individual simulations differ from each other, the average of 20 sample sets asymptotically approaches the correct value of turbulent kinetic energy in statistical steady state, trace ($V(\mathbf{k})$). **Figure 10** displays the normal and shear stress profiles resulting from DNS and from stochastic linear simulations. The averaged output of the 20 simulations agrees well with DNS results. This agreement can be further improved by running additional simulations and by increasing the total simulation times.

5.3. Spatiotemporal Energy Spectrum

To analyze the spatiotemporal aspect of dynamical models resulting from the framework of Section 4.2, we examine the power spectral density and energy spectrum of velocity fluctuations. The power spectral density of the LTI system in Equation 22 is determined by the sum of squares of the singular values of the frequency response matrix in Equation 21:

$$\Pi_{\mathbf{v}}(\mathbf{k}, \omega) = \text{trace}\left(T_{\mathbf{vw}}(\mathbf{k}, \omega)\, T_{\mathbf{vw}}^*(\mathbf{k}, \omega)\right) = \sum_i \sigma_i^2\left(T_{\mathbf{vw}}(\mathbf{k}, \omega)\right).$$
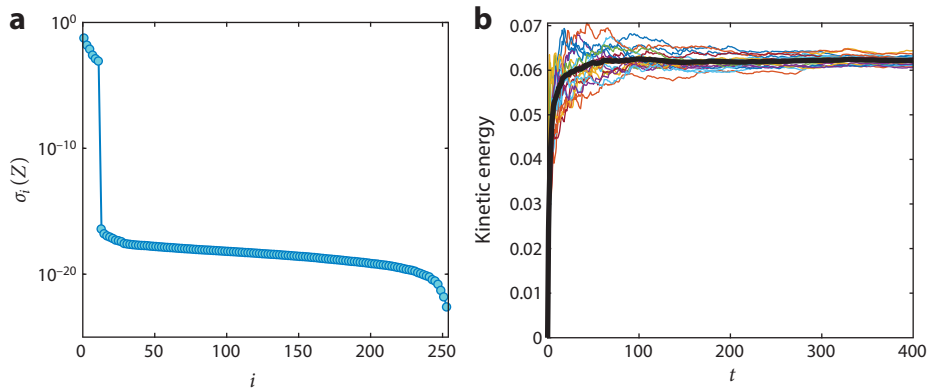
Figure 9

(*a*) Singular values of the solution Z to Equation 17 in turbulent channel flow with $Re = 186$, $\mathbf{k} = (2.5, 7)$, and $N = 127$ for $\gamma = 10^4$. (*b*) Time evolution of fluctuations' kinetic energy for 20 realizations of the stochastic input to the resulting modified linearized dynamics in Problem 1. The thick black line shows the energy averaged over all simulations. Figure adapted from Reference 55 with permission.
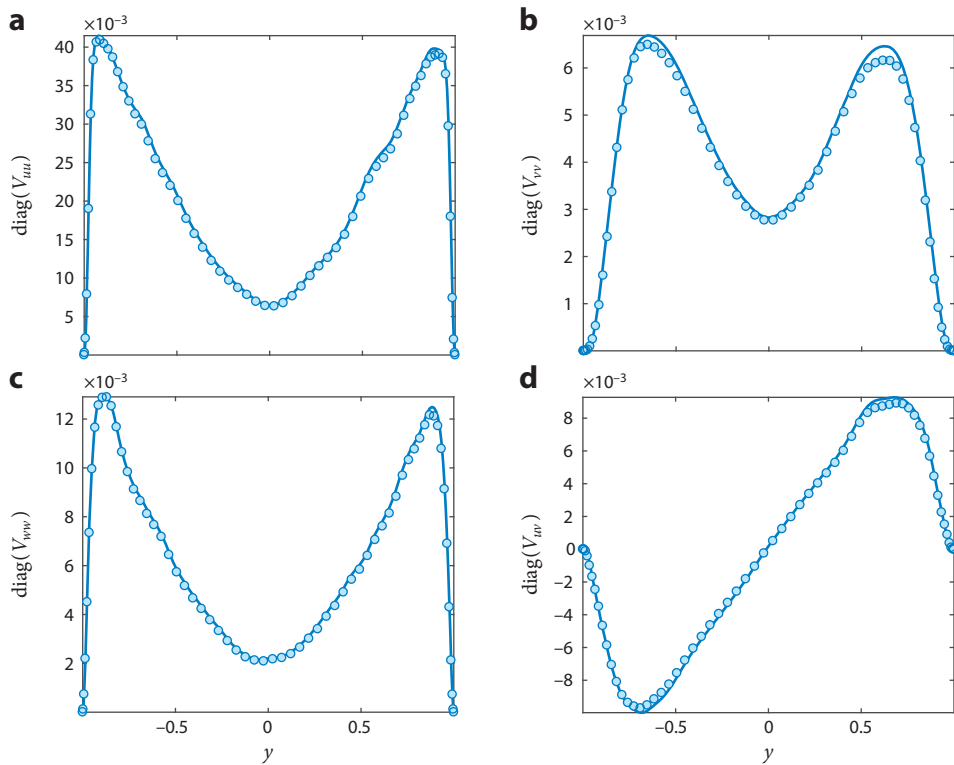

Figure 10

Normal stress profiles in (*a*) the streamwise direction, (*b*) the wall-normal direction, and (*c*) the spanwise direction, along with (*d*) the shear stress profile resulting from direct numerical simulation of turbulent channel flow with $Re = 186$ at $\mathbf{k} = (2.5, 7)$ (*line*) and stochastic linear simulations (*circles*). Figure adapted from Reference 55 with permission.
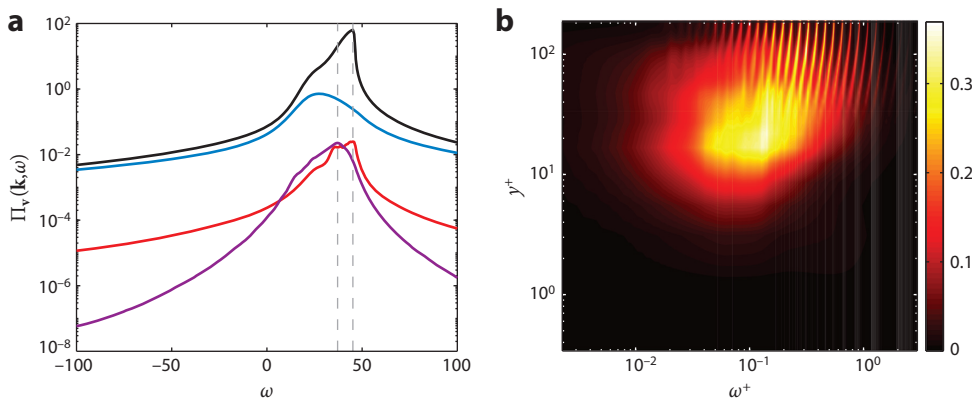
Figure 11

(*a*) Power spectral density $\Pi_{\mathbf{v}}(\mathbf{k}, \omega)$ resulting from direct numerical simulation of turbulent channel flow with $Re = 186$ at $\mathbf{k} = (2.5, 7)$ (*purple*), the linearized Navier–Stokes model in Equation 5 (*black*), an eddy-viscosity-enhanced linearized model (*blue*), and the modified linear time-invariant dynamics in Equation 22 for $\gamma = 300$ (*red*). (*b*) Premultiplied energy spectrum of the modified dynamics in Equation 22 for turbulent channel flow with $Re = 186$ resulting from the integration of $\omega \, \mathrm{diag}\,(T_{\mathbf{vw}}(\mathbf{k}, \omega)T_{\mathbf{vw}}^{*}(\mathbf{k}, \omega))$ over wavenumbers $\mathbf{k}$.

Integration of $\Pi_{\mathbf{v}}(\mathbf{k}, \omega)$ over the temporal frequencies yields the square of the H_2 norm of the system in Equation 22 or, equivalently, the $\mathbf{k}$-parameterized energy spectrum (31):

$$E(\mathbf{k}) = \frac{1}{2} \int_{-\infty}^{\infty} \Pi_{\mathbf{v}}(\mathbf{k}, \omega) \, \mathrm{d}\omega = \frac{1}{2} \, \mathrm{trace}\,(V(\mathbf{k})).$$

For a turbulent channel flow with $Re = 186$ and $\mathbf{k} = (2.5, 7)$, **Figure 11a** compares the power spectral densities of the linearized NS model given by Equation 5, the eddy-viscosity-enhanced modification of the linearized NS equations (48, 88–91), and the dynamical model given by Equation 22 resulting from the framework presented in Section 4.2 with the result of DNS. For the first two models, the input matrix $B(\mathbf{k})$ excites all degrees of freedom in the state equation, and for the modified dynamics, the input matrix $B(\mathbf{k})$ comes from the framework presented in Section 4.2 with the regularization parameter $\gamma = 300$. All three models are driven by spatially and temporally uncorrelated inputs.

The temporal frequency at which the power spectral density peaks is similar for the linearized NS equations and the modified dynamics ($\omega \approx 45$) and is closer to the result of DNS ($\omega \approx 37$) than the frequency associated with the eddy-viscosity-enhanced model ($\omega \approx 27$). We also see that both the eddy-viscosity enhancement and the data-driven low-rank modification attenuate the amplification of disturbances at all temporal frequencies. The uniform damping of the power spectral density ensures that the H_2 norm of the system in Equation 22 matches the energy spectrum of the turbulent channel flow (red and purple curves in **Figure 11a**). For the modified dynamics given by Equation 22, **Figure 11b** shows the premultiplied spatiotemporal energy spectrum as a function of the wall-normal coordinate and temporal frequency in inner (viscous) units, i.e., $y^{+} := (1 + y)Re$ and $\omega^{+} := \omega/Re$. This spectrum is computed by integrating $\omega \, \mathrm{diag}\,(T_{\mathbf{vw}}(\mathbf{k}, \omega)T_{\mathbf{vw}}^{*}(\mathbf{k}, \omega))$ over $\mathbf{k}$ and is concentrated around $y^{+} \approx 15$ within a frequency band $\omega^{+} \in (0.01, 1)$, which is in agreement with the trends observed in DNS-generated energy spectra (81). Improving the accuracy in matching the temporal correlations resulting from DNS may require closer examination of the role of parameter γ or the addition of extra constraints in Problem 1 and is a subject of ongoing research.

6. CONCLUDING REMARKS

This review has discussed a framework that combines tools from systems theory and optimization to develop low-complexity models of turbulent flows that are well suited for analysis and control synthesis. The goal is to embed partially known statistical signatures obtained via numerical simulation of the NS equations or experimental measurements into first-principles models that arise from linearization around the turbulent mean velocity. This amounts to identifying the spectral content of stochastic excitation into the linearized equations such that turbulent statistics can be reproduced. The review focused on the completion of second-order statistics, and while the methodology and theoretical framework are applicable to a wide range of scenarios, a channel flow configuration was used to solidify the discussion. On par with the dramatic upswing in the fields of machine learning and optimization in leveraging big data for modeling, the proposed methodology utilizes data to refine the predictive capability of a dynamical model that arises from first principles and offers a new perspective on tackling issues of robustness and generalizability.

SUMMARY POINTS

1. Data from numerical simulations and experiments can be used to refine the predictive power of models that arise from first principles, e.g., the linearized Navier–Stokes equations.

2. White-in-time stochastic input to the linearized Navier–Stokes equations cannot explain second-order statistics of turbulent wall-bounded flows.

3. Colored-in-time stochastic input that excites all degrees of freedom can completely cancel the original dynamics and yield a model that does not generalize well.

4. A suitably regularized solution to covariance completion problems can ensure that important features of spatiotemporal responses are captured via low-complexity stochastic dynamical models.

5. The effect of colored-in-time stochastic input can be equivalently interpreted as a structural perturbation of the linearized dynamical generator, which can be used to identify important state-feedback interactions that are lost through linearization.

6. Combining tools and ideas from systems theory and convex optimization can pave the way for the systematic development of theory and techniques that combine data-driven with physics-based modeling.

FUTURE ISSUES

1. Modeling of flow disturbances plays an important role in obtaining well-posed estimation gains (92, 93). Stochastic dynamical models that are obtained via covariance completion fit nicely into a Kalman filtering framework for turbulent flows and have the potential to open the door for a successful output-feedback design at higher Reynolds numbers than current feedback (8, 94, 95) and sensor-free (87, 96–99) strategies allow. The efficacy of such an approach and its interplay with real-time estimation and feedback control are yet to be examined.

2. Turbulence modeling for complex fluids and flows in complex geometries (100–107) requires dealing with a large number of degrees of freedom. Since improving upon current algorithms that require $O(n^3)$ computations for a model with n states is challenging, a possible direction is to examine physical approximations (108–111) and model reduction techniques (13, 15–17).

3. The regularization terms in Problems 1 and 2 are used as convex surrogates for rank and cardinality. For problems with structural constraints, such surrogates do not enjoy standard probabilistic guarantees (112), and the utility of more refined approximation techniques—e.g., manifold optimization (113), low-rank-inducing norms (114, 115), and nonconvex matrix completion (116–118)—in low-complexity stochastic dynamical modeling remains largely unexplored.

4. Higher-order turbulent flow statistics often play an important role in characterizing quantities of interest in engineering applications; e.g., fourth-order statistics are relevant in acoustic source modeling for high-speed jets (119, 120). The importance of matching higher-order statistics calls for a generalized theory for the stochastic realization of state statistics that are currently limited to second-order correlations.

5. The output of the stochastically forced linear model can be used to drive the mean flow equations in time-dependent stochastic simulations. It is important to identify conditions under which the feedback interconnection in **Figure 1b** converges.

DISCLOSURE STATEMENT

The authors are not aware of any affiliations, memberships, funding, or financial holdings that might be perceived as affecting the objectivity of this review.

ACKNOWLEDGMENTS

LITERATURE CITED

1. Joslin RD. 1998. Aircraft laminar flow control. *Annu. Rev. Fluid Mech.* 30:1–29
2. Gad-el-Hak M. 2000. *Flow Control: Passive, Active, and Reactive Flow Management*. New York: Cambridge Univ. Press
3. Choi H, Moin P. 2012. Grid-point requirements for large eddy simulation: Chapman's estimates revisited. *Phys. Fluids* 24:011702
4. Slotnick J, Khodadoust A, Alonso J, Darmofal D, Gropp W, et al. 2014. *CFD Vision 2030 study: a path to revolutionary computational aerosciences*. Tech. Rep. CR-2014-218178, Natl. Aeronaut. Space Adm., Washington, DC
5. Sagaut P. 2006. *Large Eddy Simulation for Incompressible Flows: An Introduction*. Berlin: Springer
6. Wilcox DC. 1998. *Turbulence Modeling for CFD*. La Cañada, CA: DCW Ind. 2nd ed.
7. Durbin PA, Reif BAP. 2011. *Statistical Theory and Modeling for Turbulent Flows*. Chichester, UK: Wiley
8. Kim J, Bewley TR. 2007. A linear systems approach to flow control. *Annu. Rev. Fluid Mech.* 39:383–417

9. Robinson SK. 1991. Coherent motions in the turbulent boundary layer. *Annu. Rev. Fluid Mech.* 23:601–39

10. Adrian RJ. 2007. Hairpin vortex organization in wall turbulence. *Phys. Fluids* 19:041301

11. Smits AJ, McKeon BJ, Marusic I. 2011. High–Reynolds number wall turbulence. *Annu. Rev. Fluid Mech.* 43:353–75

12. Jiménez J. 2018. Coherent structures in wall-bounded turbulence. *J. Fluid Mech.* 842:P1

13. Rowley CW. 2005. Model reduction for fluids using balanced proper orthogonal decomposition. *Int. J. Bifurc. Chaos* 15:997–1013

14. Lumley JL. 2007. *Stochastic Tools in Turbulence*. Mineola, NY: Dover

15. Schmid PJ. 2010. Dynamic mode decomposition of numerical and experimental data. *J. Fluid Mech.* 656:5–28

16. Jovanović MR, Schmid PJ, Nichols JW. 2014. Sparsity-promoting dynamic mode decomposition. *Phys. Fluids* 26:024103

17. Rowley CW, Dawson ST. 2017. Model reduction for flow analysis and control. *Annu. Rev. Fluid Mech.* 49:387–417

18. Towne A, Schmidt OT, Colonius T. 2018. Spectral proper orthogonal decomposition and its relationship to dynamic mode decomposition and resolvent analysis. *J. Fluid Mech.* 847:821–67

19. Noack BR, Morzyński M, Tadmor G. 2011. *Reduced-Order Modelling for Flow Control*. New York: Springer

20. Tadmor G, Noack BR. 2011. Bernoulli, Bode, and Budgie. *IEEE Control Syst. Mag.* 31(2):18–23

21. Trefethen LN, Trefethen AE, Reddy SC, Driscoll TA. 1993. Hydrodynamic stability without eigenvalues. *Science* 261:578–84

22. Schmid PJ. 2007. Nonmodal stability theory. *Annu. Rev. Fluid Mech.* 39:129–62

23. Gustavsson LH. 1991. Energy growth of three-dimensional disturbances in plane Poiseuille flow. *J. Fluid Mech.* 224:241–60

24. Butler KM, Farrell BF. 1992. Three-dimensional optimal perturbations in viscous shear flow. *Phys. Fluids A* 4:1637

25. Reddy SC, Henningson DS. 1993. Energy growth in viscous channel flows. *J. Fluid Mech.* 252:209–38

26. Henningson DS, Reddy SC. 1994. On the role of linear mechanisms in transition to turbulence. *Phys. Fluids* 6:1396–98

27. Schmid PJ, Henningson DS. 1994. Optimal energy density growth in Hagen-Poiseuille flow. *J. Fluid Mech.* 277:197–225

28. Farrell BF, Ioannou PJ. 1993. Stochastic forcing of the linearized Navier-Stokes equations. *Phys. Fluids A* 5:2600–9

29. Bamieh B, Dahleh M. 2001. Energy amplification in channel flows with stochastic excitation. *Phys. Fluids* 13:3258–69

30. Jovanović MR. 2004. *Modeling, analysis, and control of spatially distributed systems*. PhD Thesis, Univ. Calif., Santa Barbara

31. Jovanović MR, Bamieh B. 2005. Componentwise energy amplification in channel flows. *J. Fluid Mech.* 534:145–83

32. Ran W, Zare A, Hack MJP, Jovanović MR. 2019. Stochastic receptivity analysis of boundary layer flow. *Phys. Rev. Fluids* 4:093901

33. Butler KM, Farrell BF. 1993. Optimal perturbations and streak spacing in wall-bounded turbulent shear flow. *Phys. Fluids A* 5:774–77

34. Farrell BF, Ioannou PJ. 1993. Optimal excitation of three-dimensional perturbations in viscous constant shear flow. *Phys. Fluids A* 5:1390–400

35. Farrell BF, Ioannou PJ. 1998. Perturbation structure and spectra in turbulent channel flow. *Theor. Comput. Fluid Dyn.* 11:237–50

36. McKeon BJ, Sharma AS. 2010. A critical-layer framework for turbulent pipe flow. *J. Fluid Mech.* 658:336–82

37. Moarref R, Sharma AS, Tropp JA, McKeon BJ. 2013. Model-based scaling of the streamwise energy density in high-Reynolds-number turbulent channels. *J. Fluid Mech.* 734:275–316

38. Moarref R, Jovanović MR, Tropp JA, Sharma AS, McKeon BJ. 2014. A low-order decomposition of turbulent channel flow via resolvent analysis and convex optimization. *Phys. Fluids* 26:051701

39. McComb WD. 1991. *The Physics of Fluid Turbulence*. Oxford, UK: Oxford Univ. Press

40. Kraichnan RH. 1959. The structure of isotropic turbulence at very high Reynolds numbers. *J. Fluid Mech.* 5:497–543

41. Kraichnan RH. 1971. An almost-Markovian Galilean-invariant turbulence model. *J. Fluid Mech.* 47:513–24

42. Orszag SA. 1970. Analytical theories of turbulence. *J. Fluid Mech.* 41:363–86

43. Monin AS, Yaglom AM. 1975. *Statistical Fluid Mechanics: Mechanics of Turbulence*, Vol. 2. Cambridge, MA: MIT Press

44. Farrell BF, Ioannou PJ. 1993. Stochastic dynamics of baroclinic waves. *J. Atmos. Sci.* 50:4044–57

45. Farrell BF, Ioannou PJ. 1994. A theory for the statistical equilibrium energy spectrum and heat flux produced by transient baroclinic waves. *J. Atmos. Sci.* 51:2685–98

46. DelSole T, Farrell BF. 1995. A stochastically excited linear system as a model for quasigeostrophic turbulence: analytic results for one- and two-layer fluids. *J. Atmos. Sci.* 52:2531–47

47. Hwang Y, Cossu C. 2010. Amplification of coherent streaks in the turbulent Couette flow: an input-output analysis at low Reynolds number. *J. Fluid Mech.* 643:333–48

48. Hwang Y, Cossu C. 2010. Linear non-normal energy amplification of harmonic and stochastic forcing in the turbulent channel flow. *J. Fluid Mech.* 664:51–73

49. Jovanović MR, Bamieh B. 2001. Modelling flow statistics using the linearized Navier-Stokes equations. In *Proceedings of the 40th IEEE Conference on Decision and Control*, Vol. 5, pp. 4944–49. Piscataway, NJ: IEEE

50. Pope SB. 2000. *Turbulent Flows*. Cambridge, UK: Cambridge Univ. Press

51. Jones W, Launder B. 1972. The prediction of laminarization with a two-equation model of turbulence. *Int. J. Heat Mass Transf.* 15:301–14

52. Launder B, Sharma B. 1974. Application of the energy-dissipation model of turbulence to the calculation of flow near a spinning disc. *Lett. Heat Mass Transf.* 1:131–37

53. Kim J, Moin P, Moser R. 1987. Turbulence statistics in fully developed channel flow at low Reynolds number. *J. Fluid Mech.* 177:133–66

54. Weideman JAC, Reddy SC. 2000. A MATLAB differentiation matrix suite. *ACM Trans. Math. Softw.* 26:465–519

55. Zare A, Jovanović MR, Georgiou TT. 2017. Colour of turbulence. *J. Fluid Mech.* 812:636–80

56. Malkus WVR. 1956. Outline of a theory of turbulent shear flow. *J. Fluid Mech.* 1:521–39

57. Reynolds WC, Tiederman WG. 1967. Stability of turbulent channel flow with application to Malkus's theory. *J. Fluid Mech.* 27:253–72

58. Georgiou TT. 2002. Spectral analysis based on the state covariance: the maximum entropy spectrum and linear fractional parametrization. *IEEE Trans. Autom. Control* 47:1811–23

59. Georgiou TT. 2002. The structure of state covariances and its relation to the power spectrum of the input. *IEEE Trans. Autom. Control* 47:1056–66

60. Moin P, Moser R. 1989. Characteristic-eddy decomposition of turbulence in a channel. *J. Fluid Mech.* 200:471–509

61. Zare A, Chen Y, Jovanović MR, Georgiou TT. 2017. Low-complexity modeling of partially available second-order statistics: theory and an efficient matrix completion algorithm. *IEEE Trans. Autom. Control* 62:1368–83

62. Chen Y, Jovanović MR, Georgiou TT. 2013. State covariances and the matrix completion problem. In *52nd IEEE Conference on Decision and Control*, pp. 1702–7. Piscataway, NJ: IEEE

63. Boyd S, Vandenberghe L. 2004. *Convex Optimization*. Cambridge, UK: Cambridge Univ. Press

64. Goodwin GC, Payne RL. 1977. *Dynamic System Identification: Experiment Design and Data Analysis*. New York: Academic

65. Fazel M. 2002. *Matrix rank minimization with applications*. PhD Thesis, Stanford Univ., Stanford, CA

66. Recht B, Fazel M, Parrilo PA. 2010. Guaranteed minimum-rank solutions of linear matrix equations via nuclear norm minimization. *SIAM Rev.* 52:471–501

67. Hotz A, Skelton RE. 1987. Covariance control theory. *Int. J. Control* 46:13–32

68. Yasuda K, Skelton RE, Grigoriadis KM. 1993. Covariance controllers: a new parametrization of the class of all stabilizing controllers. *Automatica* 29:785–88

69. Grigoriadis KM, Skelton RE. 1994. Alternating convex projection methods for covariance control design. *Int. J. Control* 60:1083–106

70. Chen Y, Georgiou TT, Pavon M. 2016. Optimal steering of a linear stochastic system to a final probability distribution, part II. *IEEE Trans. Autom. Control* 61:1170–80

71. Lin F, Jovanović MR. 2009. Least-squares approximation of structured covariances. *IEEE Trans. Autom. Control* 54:1643–48

72. Zorzi M, Ferrante A. 2012. On the estimation of structured covariance matrices. *Automatica* 48:2145–51

73. Zare A, Jovanović MR, Georgiou TT. 2016. Perturbation of system dynamics and the covariance completion problem. In *2016 IEEE 55th Conference on Decision and Control*, pp. 7036–41. Piscataway, NJ: IEEE

74. Zare A, Mohammadi H, Dhingra NK, Georgiou TT, Jovanović MR. 2020. Proximal algorithms for large-scale statistical modeling and sensor/actuator selection. *IEEE Trans. Autom. Control*. In press. **https://doi.org/10.1109/TAC.2019.2948268**

75. Zare A, Jovanović MR, Georgiou TT. 2015. Alternating direction optimization algorithms for covariance completion problems. In *2015 American Control Conference*, pp. 515–20. Piscataway, NJ: IEEE

76. Toh KC, Todd MJ, Tütüncü RH. 1999. SDPT3—a MATLAB software package for semidefinite programming, version 1.3. *Optim. Methods Softw.* 11:545–81

77. Grant M, Boyd S. 2014. CVX: Matlab software for disciplined convex programming, version 2.1. *CVX Research*. **http://cvxr.com/cvx**

78. Sasaki K, Piantanida S, Cavalieri AVG, Jordan P. 2017. Real-time modelling of wavepackets in turbulent jets. *J. Fluid Mech.* 821:458–81

79. Beneddine S, Sipp D, Arnault A, Dandois J, Lesshafft L. 2016. Conditions for validity of mean flow stability analysis. *J. Fluid Mech.* 798:485–504

80. Beneddine S, Yegavian R, Sipp D, Leclaire B. 2017. Unsteady flow dynamics reconstruction from mean flow and point sensors: an experimental study. *J. Fluid Mech.* 824:174–201

81. Towne A, Lozano-Durán A, Yang X. 2019. Resolvent-based estimation of space-time flow statistics. arXiv:1901.07478 [physics.flu-dyn]

82. Morra P, Semeraro O, Henningson DS, Cossu C. 2019. On the relevance of Reynolds stresses in resolvent analyses of turbulent wall-bounded flows. *J. Fluid Mech.* 867:969–84

83. Moser RD, Kim J, Mansour NN. 1999. DNS of turbulent channel flow up to $Re_\tau = 590$. *Phys. Fluids* 11:943–45

84. Del Álamo JC, Jiménez J. 2003. Spectra of the very large anisotropic scales in turbulent channels. *Phys. Fluids* 15:41–44

85. Del Álamo JC, Jiménez J, Zandonade P, Moser RD. 2004. Scaling of the energy spectra of turbulent channels. *J. Fluid Mech.* 500:135–44

86. Monty JP, Stewart JA, Williams RC, Chong MS. 2007. Large-scale features in turbulent pipe and channel flows. *J. Fluid Mech.* 589:147–56

87. Moarref R, Jovanović MR. 2012. Model-based design of transverse wall oscillations for turbulent drag reduction. *J. Fluid Mech.* 707:205–40

88. Reynolds WC, Hussain AKMF. 1972. The mechanics of an organized wave in turbulent shear flow. Part 3. Theoretical models and comparisons with experiments. *J. Fluid Mech.* 54:263–88

89. Del Álamo JC, Jiménez J. 2006. Linear energy amplification in turbulent channels. *J. Fluid Mech.* 559:205–13

90. Cossu C, Pujals G, Depardon S. 2009. Optimal transient growth and very large-scale structures in turbulent boundary layers. *J. Fluid Mech.* 619:79–94

91. Pujals G, García-Villalba M, Cossu C, Depardon S. 2009. A note on optimal transient growth in turbulent channel flows. *Phys. Fluids* 21:015109

92. Hœpffner J, Chevalier M, Bewley TR, Henningson DS. 2005. State estimation in wall-bounded flow systems. Part 1. Perturbed laminar flows. *J. Fluid Mech.* 534:263–94

93. Chevalier M, Hœpffner J, Bewley TR, Henningson DS. 2006. State estimation in wall-bounded flow systems. Part 2. Turbulent flows. *J. Fluid Mech.* 552:167–87

94. Bewley TR, Liu S. 1998. Optimal and robust control and estimation of linear paths to transition. *J. Fluid Mech.* 365:305–49

95. Högberg M, Bewley TR, Henningson DS. 2003. Linear feedback control and estimation of transition in plane channel flow. *J. Fluid Mech.* 481:149–75

96. Fransson JHM, Talamelli A, Brandt L, Cossu C. 2006. Delaying transition to turbulence by a passive mechanism. *Phys. Rev. Lett.* 96:064501

97. Jovanović MR. 2008. Turbulence suppression in channel flows by small amplitude transverse wall oscillations. *Phys. Fluids* 20:014101

98. Moarref R, Jovanović MR. 2010. Controlling the onset of turbulence by streamwise traveling waves. Part 1: receptivity analysis. *J. Fluid Mech.* 663:70–99

99. Lieu BK, Moarref R, Jovanović MR. 2010. Controlling the onset of turbulence by streamwise traveling waves. Part 2: direct numerical simulations. *J. Fluid Mech.* 663:100–19

100. Hoda N, Jovanović MR, Kumar S. 2008. Energy amplification in channel flows of viscoelastic fluids. *J. Fluid Mech.* 601:407–24

101. Hoda N, Jovanović MR, Kumar S. 2009. Frequency responses of streamwise-constant perturbations in channel flows of Oldroyd-B fluids. *J. Fluid Mech.* 625:411–34

102. Jovanović MR, Kumar S. 2010. Transient growth without inertia. *Phys. Fluids* 22:023101

103. Jovanović MR, Kumar S. 2011. Nonmodal amplification of stochastic disturbances in strongly elastic channel flows. *J. Non-Newton. Fluid Mech.* 166:755–78

104. Lieu BK, Jovanović MR, Kumar S. 2013. Worst-case amplification of disturbances in inertialess Couette flow of viscoelastic fluids. *J. Fluid Mech.* 723:232–63

105. Jeun J, Nichols JW, Jovanović MR. 2016. Input-output analysis of high-speed axisymmetric isothermal jet noise. *Phys. Fluids* 28:047101

106. Hildebrand N, Dwivedi A, Nichols JW, Jovanović MR, Candler GV. 2018. Simulation and stability analysis of oblique shock wave/boundary layer interactions at Mach 5.92. *Phys. Rev. Fluids* 3:013906

107. Dwivedi A, Sidharth GS, Nichols JW, Candler GV, Jovanović MR. 2019. Reattachment vortices in hypersonic compression ramp flow: an input-output analysis. *J. Fluid Mech.* 880:113–35

108. Reed HL, Saric WS, Arnal D. 1996. Linear stability theory applied to boundary layers. *Annu. Rev. Fluid Mech.* 28:389–428

109. Herbert T. 1997. Parabolized stability equations. *Annu. Rev. Fluid Mech.* 29:245–83

110. Högberg M, Henningson DS. 2002. Linear optimal control applied to instabilities in spatially developing boundary layers. *J. Fluid Mech.* 470:151–79

111. Ran W, Zare A, Hack MJP, Jovanović MR. 2019. Modeling mode interactions in boundary layer flows via parabolized Floquet equations. *Phys. Rev. Fluids* 4:023901

112. Candès EJ, Recht B. 2009. Exact matrix completion via convex optimization. *Found. Comput. Math.* 9:717–72

113. Absil PA, Mahony R, Sepulchre R. 2008. *Optimization Algorithms on Matrix Manifolds.* Princeton, NJ: Princeton Univ. Press

114. Grussler C, Zare A, Jovanović MR, Rantzer A. 2016. The use of the $r*$ heuristic in covariance completion problems. In *2016 IEEE 55th Conference on Decision and Control*, pp. 1978–83. Piscataway, NJ: IEEE

115. Grussler C, Rantzer A, Giselsson P. 2018. Low-rank optimization with convex constraints. *IEEE Trans. Autom. Control* 63:4000–7

116. Candes EJ, Li X, Soltanolkotabi M. 2015. Phase retrieval via Wirtinger flow: theory and algorithms. *IEEE Trans. Inf. Theory* 61:1985–2007

117. Sun R, Luo ZQ. 2016. Guaranteed matrix completion via non-convex factorization. *IEEE Trans. Inf. Theory* 62:6535–79

118. Ge R, Lee JD, Ma T. 2016. Matrix completion has no spurious local minimum. In *Advances in Neural Information Processing Systems 29*, ed. DD Lee, M Sugiyama, UV Luxburg, I Guyon, R Garnett, pp. 2973–81. Red Hook, NY: Curran

119. Karabasov SA, Afsar MZ, Hynes TP, Dowling AP, McMullan WA, et al. 2010. Jet noise: acoustic analogy informed by large eddy simulation. *AIAA J.* 48:1312–25

120. Leib SJ, Goldstein ME. 2011. Hybrid source model for predicting high-speed jet noise. *AIAA J.* 49:1324–35

Contents

Errata

An online log of corrections to *Annual Review of Control, Robotics, and Autonomous
Systems* articles may be found at http://www.annualreviews.org/errata/control